Obrabotka metallov (tekhnologiya, oborudovanie, instrumenty) = Metal Working and Material Science. 2026 vol. 28 no. 3 pp. 250–268
ISSN: 1994-6309 (print) / 2541-819X (online)
DOI: 10.17212/1994-6309-2026-28.3-250-268

NSTU NETI

Obrabotka metallov - Metal Working and Material Science

Journal homepage: http://journals.nstu.ru/obrabotka_metallov

Effect of carbon alloying and heat treatment on the microstructure, mechanical properties, and tribological behaviour of a powder-metallurgy CoCrCuFeNi high-entropy alloy (HEA)

Pavel Loginov [1, 2, a, *], ***Alexander Fedotov*** [1, b], ***Samat Mukanov*** [1, c], ***Bogdan Romanenko*** [1, d], ***Yulia Chkannikova*** [1, e], ***Nikita Koltsov*** [1, f], ***Marina Bychkova*** [1, j], ***Olga Manakova*** [1, h]

[1] National University of Science and Technology MISIS, 4 Leninsky Prospekt, building 1, Moscow, 119049, Russian Federation
[2] Institute of Nanotechnology of Microelectronics of the Russian Academy of Sciences, 32A Leninsky Prospekt, Moscow, 119334, Russian Federation

[a] https://orcid.org/0000-0003-2505-2918, pavel.loginov.misis@list.ru; [b] https://orcid.org/0009-0009-9208-1453, sashok12221998@mail.ru;
[c] https://orcid.org/0000-0001-6719-6237, smukanov@misis.ru; [d] https://orcid.org/0009-0003-7470-5185, a.v.d.romanenko@gmail.com;
[e] https://orcid.org/0009-0006-5211-8993, firestorm567@bk.ru; [f] https://orcid.org/0009-0007-5410-5915, koltsov02@mail.ru;
[j] https://orcid.org/0000-0002-9233-4707, bychkova@shs.misis.ru; [h] https://orcid.org/0000-0001-8882-4191, manakova_ol@mail.ru

ARTICLE INFO

Article history:
Received: 14 May 2026
Revised: 25 May 2026
Accepted: 17 July 2026
Available online: 15 September 2026

Keywords:
High-entropy alloys
Powder metallurgy
Mechanical properties
Tribological properties
Strengthening mechanism

Funding
This study was funded by the Russian Science Foundation (Project No. 22-79-10144-P).

Acknowledgments
The authors express their sincere gratitude to M.I. Petrzhik, Head of the Functional Surfaces Testing Laboratory at NUST MISIS, for assistance with the mechanical property characterization.

ABSTRACT

Introduction. Powder metallurgy high-entropy alloys (*HEAs*) of the *CoCrCuFeNi* system exhibit high strength but low ductility due to their ultrafine-grained structure and inhomogeneous distribution of the copper-rich phase. One approach to improve the balance of mechanical properties involves the microaddition of non-metallic elements, particularly carbon, which can enhance both strength and ductility. ***The purpose of this study*** is to determine the effect of carbon content (0.2–1.0 wt.%) and heat treatment on the phase composition, microstructure, mechanical properties, and tribological behavior of powder metallurgy CoCrCuFeNi HEAs fabricated by mechanical alloying and hot pressing. **Materials and methods.** The investigation employed X-ray diffraction (*XRD*), scanning electron microscopy (*SEM*), transmission electron microscopy (*TEM*), hardness testing, bending testing, tensile testing, and pin-on-plate tribological testing (with Si_3N_4 as the counterbody). **Results and discussion.** It is established that carbon is bound into $Cr_{23}C_6$ and $Cr_2(C,N)$ phases without altering the ratio of the major phases. Hardness increase from 3.27 to 3.56 GPa, and bending strength increased from 1,440 to 1,620 MPa. For the alloy containing 1.0 wt.% *C* after annealing, a bending strength of 1,780 MPa, a tensile strength of 1,010 MPa, and an elongation of 2.3% were achieved, whereas the base alloy exhibited brittle fracture at 730 MPa. *TEM* analysis revealed that carbides are predominantly located at grain boundaries of the matrix (grain size 620–840 nm), facilitating a transition from intergranular cleavage to ductile dimple fracture. The friction coefficient (0.75–0.77) is weakly dependent on composition, while the lowest wear is attained after annealing of the carbon-alloyed composition. It is found that alloying with carbon (1.0 wt.%) followed by heat treatment enhances both the strength and ductility of powder metallurgy *CoCrCuFeNi HEAs* through carbide strengthening and optimization of grain boundary structure.

For citation: Loginov P.A., Fedotov A.D., Mukanov S.K., Romanenko B.Yu., Chkannikova Yu.G., Koltsov N.A., Bychkova M.Ya., Manakova O.S. Effect of carbon alloying and heat treatment on the microstructure, mechanical properties, and tribological behaviour of a powder-metallurgy CoCrCuFeNi high-entropy alloy (HEA). *Obrabotka metallov (tekhnologiya, oborudovanie, instrumenty) = Metal Working and Material Science*, 2026, vol. 28, no. 3, pp. 250–268. DOI: 10.17212/1994-6309-2026-28.3-250-268. (In Russian).

Introduction

The concept of high-entropy alloys (*HEAs*), which assumes the formation of multi-component solid solutions without a dominant element, has introduced a new approach to materials design and opened up the central region of multi-component phase diagrams for research [1, 2]. These alloys, which consist of four or

*** Corresponding author**
Loginov Pavel Alexandrovich, D.Sc. (Engineering), Associate Professor
National University of Science and Technology MISIS,
4 Leninsky Prospekt, Bldg. 1,
119049, Moscow, Russian Federation
Tel.: +7 916 695-68-07, **e-mail:** pavel.loginov.misis@list.ru

more principal elements in near-equimolar ratios, exhibit, contrary to traditional alloying logic, the stability of simple crystal lattices (e.g., *FCC* or *BCC*), despite their high chemical complexity.

Of particular interest are *HEAs* with a face-centered cubic (*FCC*) lattice, which attract researchers' attention due to their exceptional potential for combining mutually exclusive mechanical properties – high strength and ductility [3–5]. This unique combination arises from the synergistic interplay of several phenomena: solid solution strengthening caused by lattice distortions, complex dislocation dynamics in a chemically inhomogeneous environment, and the possibility of activating additional deformation mechanisms, such as twinning-induced plasticity (*TWIP*) and transformation-induced plasticity (*TRIP*) [6, 7].

Among *FCC*-type *HEAs*, alloys of the *Co–Cr–Cu–Fe–Ni* system are of particular interest due to several distinctive features. These alloys can be consolidated by powder metallurgy methods to a nearly pore-free state at relatively low temperatures (1,000 °C). They have proven to be effective as a matrix material for diamond-containing composites, since they simultaneously provide high adhesion to diamond, protection against graphitization, and high fracture toughness [8, 9]. *CoCrCuFeNi* coatings exhibit excellent tribocorrosion performance and offer corrosion protection for structures operating in seawater [10, 11]. *CoCrCuFeNi HEAs* are also used as antibacterial materials [12] and in other application fields.

The presence of a copper-enriched phase in *Co–Cr–Cu–Fe–Ni HEAs*, which forms as a result of decomposition of the supersaturated *FCC* solid solution, leads to a reduction in the strength of cast alloys due to the formation of a continuous soft interdendritic network [13, 14]. Such alloys exhibit fairly high ductility but low strength, which is attributed to the dominant influence of the *Cu*-phase. In powder metallurgy *Co–Cr–Cu–Fe–Ni HEAs*, by contrast, the strength is relatively high (*UTS* ≈ 700–800 MPa) while ductility is low. This is explained by the formation of a near-nanocrystalline structure, owing to sluggish diffusion in such systems [15], as well as to the heterogeneous distribution of the *Cu* phase [16, 17]. At present, the improvement of *HEAs* in the *Co–Cr–Cu–Fe–Ni* system is mainly achieved through compositional optimization, either by reducing the *Cu* content [18] or by increasing the *Ni* content, which enhances the solubility of *Cu* in the matrix solid solution [19].

Recently, solutions to specific problems of various *HEAs* have been found in their alloying with non-metallic elements: boron [20], nitrogen [21], and carbon [22], as well as in the combined application of these components.

Carbon alloying is a promising approach for increasing the overall strength and ductility of *HEAs*, particularly those of the *Co–Cr–Cu–Fe–Ni* system. In *FCC*-type *HEAs*, upon carbon addition, the strengthening effect is dominant. The main mechanisms involved are solid solution strengthening, dispersion strengthening by carbide phases, and grain boundary strengthening. Solid solution strengthening makes a substantial contribution to the increase in strength, because carbon atoms, which dissolve interstitially in the matrix lattice, greatly increase the degree of lattice distortion. This mechanism is activated at carbon concentrations of about 1% [23]. At higher concentrations, when the solubility limit in the matrix *FCC* phase is exceeded, carbon interacts with chromium, forming dispersed Cr_xC_y carbide particles that provide strengthening via the *Orowan* mechanism [24] or grain boundary pinning [25]. Several researchers have established a consistent trend of grain size reduction in carbon-alloyed *HEAs* [26, 27], which suggests the involvement of the *Hall–Petch* mechanism, providing additional strengthening.

The effect of carbon additions also extends to improving the ductility of *HEAs*, which is attributed to the change in stacking fault energy of the matrix *FCC* phase upon carbon dissolution and, consequently, to an increased tendency of the alloys toward deformation twinning [26, 28]. Despite the available data on the positive effect of carbon on the mechanical properties of *HEAs*, systematic studies on the influence of carbon additions on the structure, phase composition, and mechanical properties of powder metallurgy *Co–Cr–Cu–Fe–Ni* alloys produced by hot pressing are insufficiently represented in the literature.

The purpose of the present work is to establish the regularities of the effect of carbon content (0.2–1.0 wt.%) and subsequent heat treatment (annealing at 900 °C) on the phase composition, microstructure, mechanical properties, deformation behavior, and tribological properties of powder metallurgy *CoCrCuFeNi*-based *HEAs* produced by mechanical alloying (*MA*) and hot pressing (*HP*).

To achieve this purpose, ***the following tasks*** were formulated:

– to ensure the formation of homogeneous *CoCrCuFeNi–C* alloy particles with a uniform distribution of all elements (including carbon), instead of a mechanical mixture of individual powders, which is necessary for a correct comparison of the effect of different carbon contents on the *HEA* properties;

– to evaluate how carbon concentration and heat treatment conditions affect the mechanical property profile (hardness, bending strength, tensile strength, and residual strain), and to correlate these properties with the resulting microstructure;

– to study the deformation behavior and fracture mechanisms of carbon-alloyed *CoCrCuFeNi* alloys by analyzing deformation curves and by fractographic examination of fracture surfaces;

– to study the tribological properties (coefficient of friction and specific wear) of the obtained alloys under dry sliding against Si_3N_4 ceramic counterbody, and to establish the effect of carbon alloying and heat treatment on the wear resistance of the material.

Methods

The following initial powders were used in this work: carbonyl *Fe* (grade *VK 3*, $\boldsymbol{d} < 9$ μm, 99% purity), carbonyl *Ni* (*PNK UT3*, $\boldsymbol{d} < 10$ μm, 99% purity), reduced *Co* (*PK 1u*, $\boldsymbol{d} < 1.2$ μm, 99% purity), reduced *Cr* (*PM ERKh*, $\boldsymbol{d} < 80$ μm, 99% purity), electrolytic *Cu* (*PMS 1*, $\boldsymbol{d} < 24$ μm, 98% purity), and technical carbon black (*grade P 804T*, $\boldsymbol{d} < 0.4$ μm, 98% purity). The equiatomic *CoCrCuFeNi* alloy was chosen as the base composition and was alloyed with carbon in amounts of 0.2, 0.4, 0.6, 0.8, and 1.0 wt.%. These alloys are hereafter designated as *CoCrCuFeNi*, *CoCrCuFeNi–0.2C*, *CoCrCuFeNi–0.4C*, *CoCrCuFeNi–0.6C*, *CoCrCuFeNi–0.8C*, and *CoCrCuFeNi–1.0C*.

Powder mixtures were prepared by *MA* using a planetary centrifugal mill (*PCM*) *Activator 2sl* (*Zavod Khimicheskogo Mashinostroeniya*, Russia) under the following conditions: drum rotation speed of 694 rpm, duration of 30 min, and ball-to-powder weight ratio of 15:1. To prevent oxidation of the powders during processing, the drums were filled with argon.

Compacted specimens in the form of cylinders with a diameter of 50 mm and a height of 4 mm were obtained from the *MA* powder mixtures by *HP* using a *DSP 515 SA* press (*Dr. Fritsch*, Germany) in vacuum at a temperature of 1,000 °C, a pressure of 35 MPa, and an isobaric holding time of 3 min. Some of the specimens were subjected to additional heat treatment (*HT*) – annealing in a tube furnace in a hydrogen atmosphere at 900 °C with a holding time in the hot zone of 30 min. Hydrogen was chosen as the *HT* atmosphere because of its reducing effect on oxide phases (except Cr_2O_3), which are inevitably present in powder-processed materials.

X-ray diffraction (*XRD*) phase analysis of the powder mixtures and compact specimens was carried out on an automated *DRON 4-07* diffractometer using monochromatic *Co Kα* radiation in the *Bragg–Brentano* geometry. The microstructure and composition of the *HEAs* were examined by scanning electron microscopy (*SEM*) on an *S 3400N* microscope (*Hitachi*, Japan). Fine structure studies were performed using a *JEM 2100* transmission electron microscope (*Jeol*, Japan).

Porosity was evaluated by metallographic examination on polished unetched sections. Section images were obtained by *SEM* in secondary electron (*SE*) mode at a magnification of ×1,000 (at least 10 fields per specimen). The pore fraction was determined using *ImageJ* software by binarising the images and calculating the relative area of dark regions corresponding to pores.

Hardness was measured using a *Vickers HVS 50* hardness tester (*Time Group Inc.*, China) at a load of 10 N, with at least 10 indentations per specimen, and the obtained values were subsequently averaged.

Bending strength measurements were performed on a universal mechanical testing machine *LF 100* (*Walter + Bai*, Switzerland) in accordance with *GOST 14019-2003*. Test specimens (at least 5 per composition) had a prismatic shape with dimensions of 25 × 4 × 3 mm. The span between the supports was 18 mm. Tensile tests were carried out in accordance with *GOST 11701-84* using a universal testing machine *Instron 5966* (*Instron*, USA) on flat specimens (5 pieces) with a gauge length of 20 mm and a thickness of 2 mm, at a strain rate of 10^{-3} s^{-1}. The main mechanical properties were determined from the test results using *Bluehill* software.

Tribological tests were performed on a precision tribometer (*CSM Instruments*, Switzerland) in a ball-on-plate configuration under reciprocating motion. Sintered silicon nitride (Si_3N_4) balls with a diameter of 3 mm were used as counterbodies. The applied load was 2 N, and the linear speed was 5 cm/s. The wear track length was 6 mm, and the total sliding distance was 4,000 cycles. Fractographic examination, including wear track profile measurements and wear scar diameter measurements on the counterbody, was carried out using an optical profilometer *WYKO NT1100* (*Veeco*, USA) and an inverted optical microscope *AXIOVERT CA25* (*Carl Zeiss*, Germany).

Results and discussion

In the present work, an optimized mechanical alloying (*MA*) mode, previously established for producing equiatomic *CoCrCuFeNi* powder mixtures with a homogeneous elemental distribution, was employed to prepare powders with carbon additions [9]. The particle morphology after *MA* and the distribution of metallic components were examined by scanning electron microscopy (*SEM*) and energy-dispersive spectroscopy (*EDS*). The powders were found to have a flake-like shape, a monofractional size distribution, and an average particle size of 11 μm (Fig. 1,*a*, *b*).

XRD analysis of the powder mixtures revealed that a solid solution of all elements with an *FCC*-type structure was formed during processing in the *PCM* (Fig. 1,*c*). The presence of carbon slightly increases the lattice parameter of the solid solution (***a*** = 0.3607 nm for the *CoCrCuFeNi* composition and ***a*** = 0.3609 nm for *CoCrCuFeNi–1.0C*). This result is in good agreement with literature data [29, 30].

EDS mapping of the *CoCrCuFeNi–1.0C* powder mixture revealed a homogeneous distribution of all elements in the metallic matrix (Fig. 1,*d*). The absence of visible carbon agglomerates within the particles

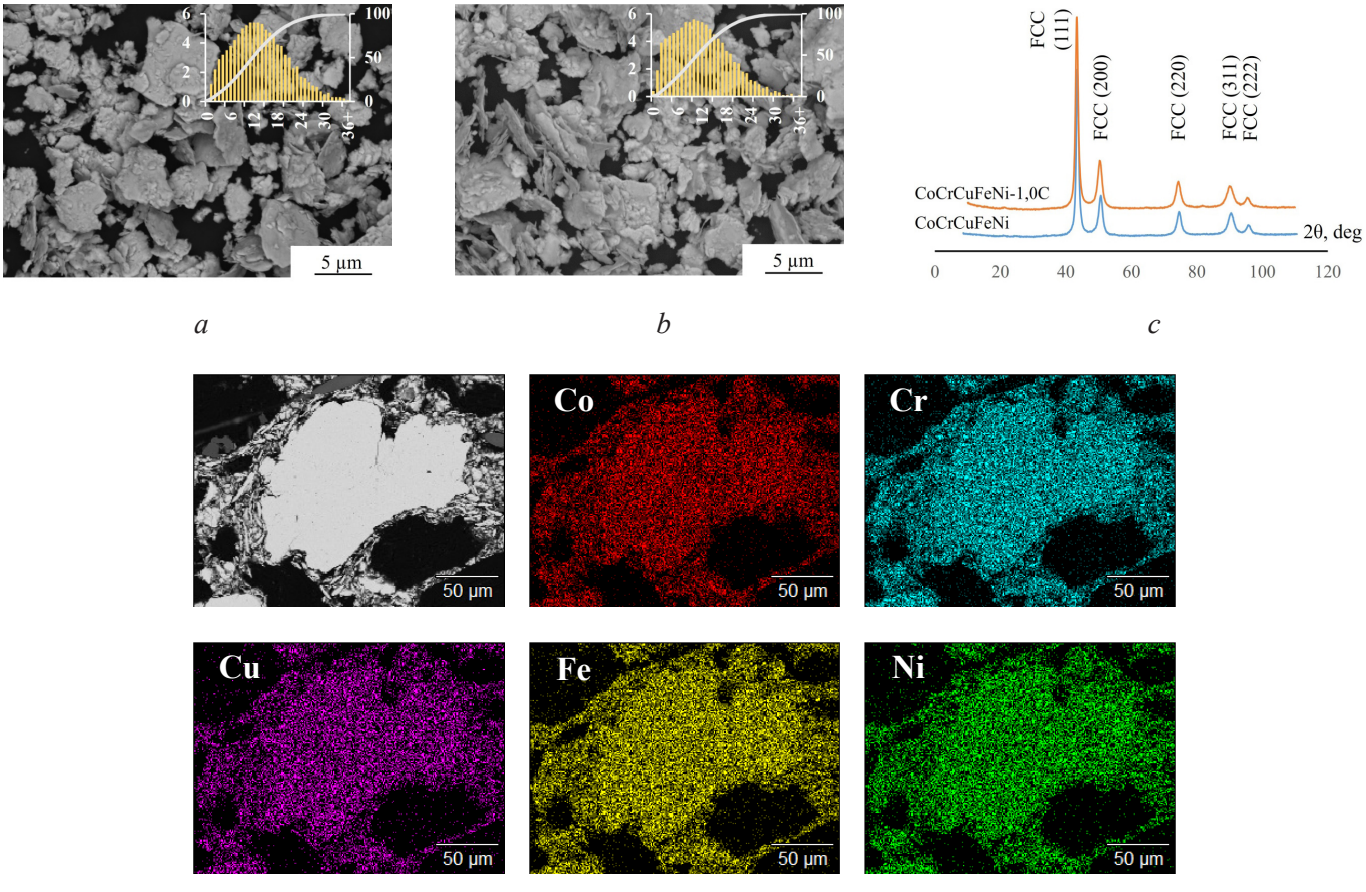

a *b* *c*

d

Fig. 1. Particle morphology of the powder mixtures of *CoCrCuFeNi* (*a*) and *CoCrCuFeNi–1.0C* (*b*) with grain-size distributions in the insets, *XRD* patterns of the *MA* powders (*c*), and elemental distribution maps for the *CoCrCuFeNi–1.0C* mixture (*d*)

suggests that carbon either dissolves in the metallic matrix during *MA*, or is at least comminuted to sizes comparable with the *SEM* resolution (several nanometers). This result differs fundamentally from the behavior of boron, another alloying addition, which dissolves interstitially in the *CoCrCuFeNi HEA*. Under the same *MA* conditions, boron does not dissolve in the matrix and remains as discrete inclusions [31].

Fig. 2 shows the *XRD* patterns of *CoCrCuFeNi* alloys with different carbon contents after *HP*, as well as after *HP* and subsequent *HT*. A two-phase structure was observed in all studied specimens. During *HP* of the base *CoCrCuFeNi* alloy, spinodal decomposition of the initial supersaturated solid solution occurs, resulting in the precipitation of a secondary *Cu*-enriched phase. This manifests itself in the *XRD* patterns as a splitting of the *FCC* phase reflections into two separate peaks. Thus, the matrix of the alloys consists of an *FCC* solid solution of all metallic components (*FCC* phase), inherited from the powder mixture, and a *Cu*-enriched phase (*Cu* phase). These results are consistent with literature data for *CoCrCuFeNi HEAs* processed by powder metallurgy [30]. The addition of carbon and subsequent *HT* do not appreciably alter the phase ratio of the *FCC* and *Cu* phases.

Carbon alloying leads to the formation of $Cr_{23}C_6$ and $Cr_2(C,N)$ phases, as confirmed by the appearance of low-intensity reflections ($Cr_2(C,N)$: $2\theta = 40.3°$ and 42.7°; $Cr_{23}C_6$ $2\theta = 33.5°$). Consequently, carbon that entered the solid solution during *MA* reacts with chromium – the element most prone to carbide formation

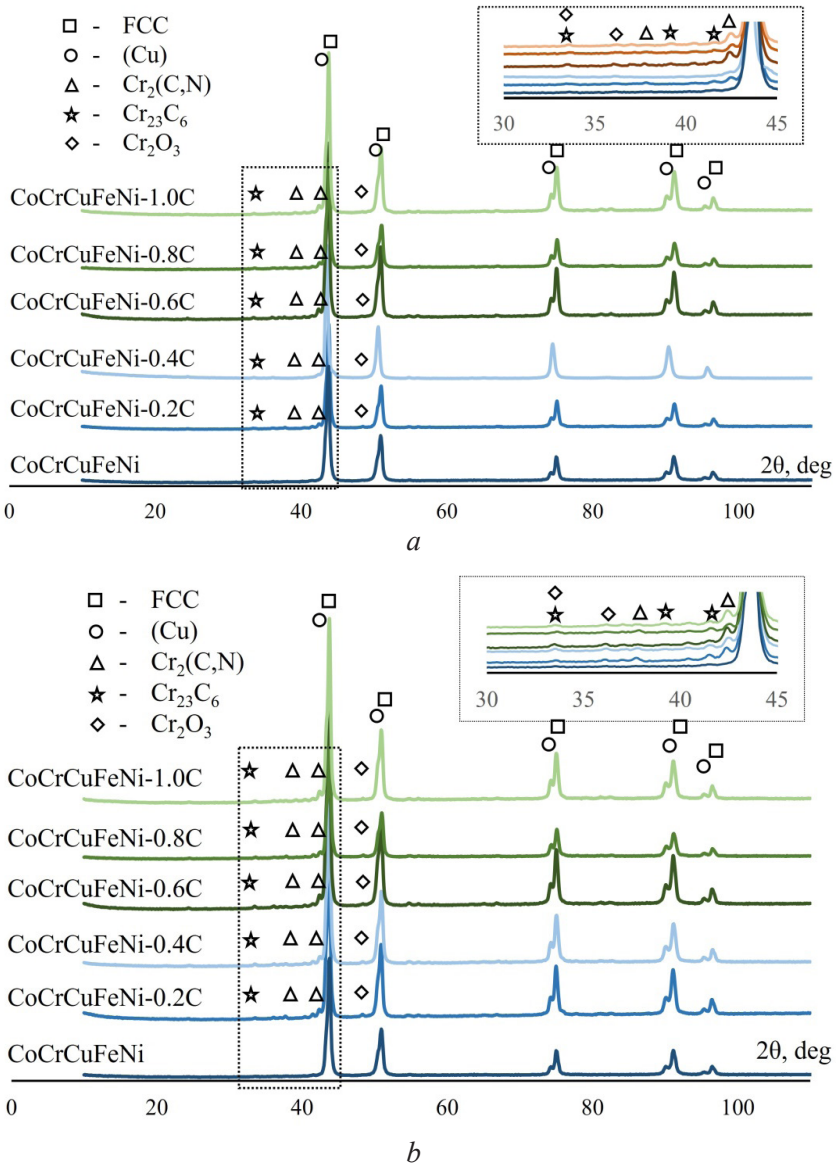

Fig. 2. X-ray diffraction patterns of *CoCrCuFeNi* with carbon addition after *HP* (*a*) and after *HP* followed by heat treatment (*b*)

in this system – during *HP*. Additional heat treatment slightly increases the carbide content, indicating that carbon is almost completely bound already at the *HP* stage. The total fraction of carbide phases does not exhibit a clear linear dependence on the carbon content in the charge and remains in the range of 3–7 wt.% for all *HEAs*. At the same time, the lattice parameter of the *FCC* matrix for all studied *HEAs* lies within a narrow range of 0.3576–0.3578 nm and shows virtually no change with increasing carbon content (Table 1). This fact indicates that the additional carbon does not enter the solid solution in interstitial positions. The lack of correlation between the carbon content, the fraction of carbide phases, and the lattice parameter may be explained by the sensitivity and accuracy limitations of the Rietveld method, or by the presence of nanosized carbides that are not identified by this technique.

Table 1

Phase composition of *CoCrCuFeNi* high-entropy alloys with carbon addition after *HP* and after *HP* followed by heat treatment

Composition	FCC	(Cu)	$Cr_2(C,N)$	$Cr_{23}C_6$	Cr_2O_3
HP					
CoCrCuFeNi	77 (***a*** = 0.3576 nm)	23 (***a*** = 0.3608 nm)			
CoCrCuFeNi–0.2C	73 (***a*** = 0.3576 nm)	23 (***a*** = 0.3608 nm)	2	2	
CoCrCuFeNi–0.4C	74 (***a*** = 0.3577 nm)	23 (***a*** = 0.3608 nm)	1	2	
CoCrCuFeNi–0.6C	73 (***a*** = 0.3577 nm)	21 (***a*** = 0.3608 nm)	3	1	2
CoCrCuFeNi–0.8C	70 (***a*** = 0.3577 nm)	23 (***a*** = 0.3609 nm)	2	3	2
CoCrCuFeNi–1.0C	73 (***a*** = 0.3577 nm)	22 (***a*** = 0.3608 nm)	3	1	1
HP + HT					
CoCrCuFeNi	77 (***a*** = 0.3578 nm)	23 (***a*** = 0.3608 nm)			
CoCrCuFeNi–0.2C	70 (***a*** = 0.3578 nm)	21 (***a*** = 0.3608 nm)	2	3	2
CoCrCuFeNi–0.4C	68 (***a*** = 0.3576 nm)	23 (***a*** = 0.3608 nm)	2	4	3
CoCrCuFeNi–0.6C	69 (***a*** = 0.3577 nm)	23 (***a*** = 0.3609 nm)	3	2	3
CoCrCuFeNi–0.8C	66 (***a*** = 0.3577 nm)	24 (***a*** = 0.3609 nm)	2	5	3
CoCrCuFeNi–1.0C	69 (***a*** = 0.3577 nm)	23 (***a*** = 0.3609 nm)	3	3	2

In addition to carbides, traces of Cr_2O_3 oxide are present in all compact specimens, which is associated with the presence of oxygen adsorbed on the surface of the starting powders.

The *Williamson–Hall* method was used to estimate the coherent scattering region (*CSR*) sizes, microstrains (**ε**), and dislocation densities (**ρ**) for all studied compositions. With increasing carbon concentration, the *CSR* size in the *HP*-processed alloys decreases, while in the *HP + HT* condition an opposite trend is observed (Table 2). The microstrains remain at a level of 0.045–0.06%, indicating that a high defect density is retained in the structure even after *HT*. The dislocation density decreases by approximately a factor of two after *HT* in all alloys, yet the values remain relatively high. It should be noted that the *CoCrCuFeNi–1.0C* alloy after *HT* exhibited the lowest dislocation density.

Fig. 3 shows SEM micrographs of the CoCrCuFeNi (*a*, *b*), *CoCrCuFeNi–0.4C* (*c*, *d*), and *CoCrCuFeNi–1.0C* (*e*, *f*) alloys in two conditions: after *HP* and after *HP* followed by heat treatment (*HP + HT*). In all specimens, the matrix is an *FCC* solid solution, which appears in the *SEM* images as regions with dark grey contrast. The size of these regions reaches several tens of micrometres. The *Cu* phase has a morphology of thin elongated irregularly shaped interlayers, the size of which varies over a wide range from 100 nm to 5 μm.

The addition of carbon up to 1.0 wt.% does not cause any noticeable changes in the microstructure: the distribution pattern of the *FCC* phase and the *Cu* phase remains unchanged. *HT* also does not induce any significant microstructural transformation; the size and morphology of the phase regions remain virtually unaltered. The residual porosity for all specimens did not exceed 1%.

Table 2

Results of *Williamson–Hall* analysis

Composition	*CSR* (nm)	**ε** (%)	**ρ** ($\times 10^{13}$ m^{-2})
HP			
CoCrCuFeNi	89.5	0.06	9.2
CoCrCuFeNi–0.2C	85.6	0.06	9.6
CoCrCuFeNi–0.4C	81.6	0.05	8.5
CoCrCuFeNi–0.6C	78.0	0.05	9.0
CoCrCuFeNi–0.8C	75.0	0.045	8.4
CoCrCuFeNi–1.0C	71.1	0.045	8.8
HP + HT			
CoCrCuFeNi	115.1	0.045	5.4
CoCrCuFeNi–0.2C	111.0	0.045	5.4
CoCrCuFeNi–0.4C	123.9	0.05	5.6
CoCrCuFeNi–0.6C	128.4	0.055	5.9
CoCrCuFeNi–0.8C	138.8	0.05	5.0
CoCrCuFeNi–1.0C	146.1	0.05	4.7

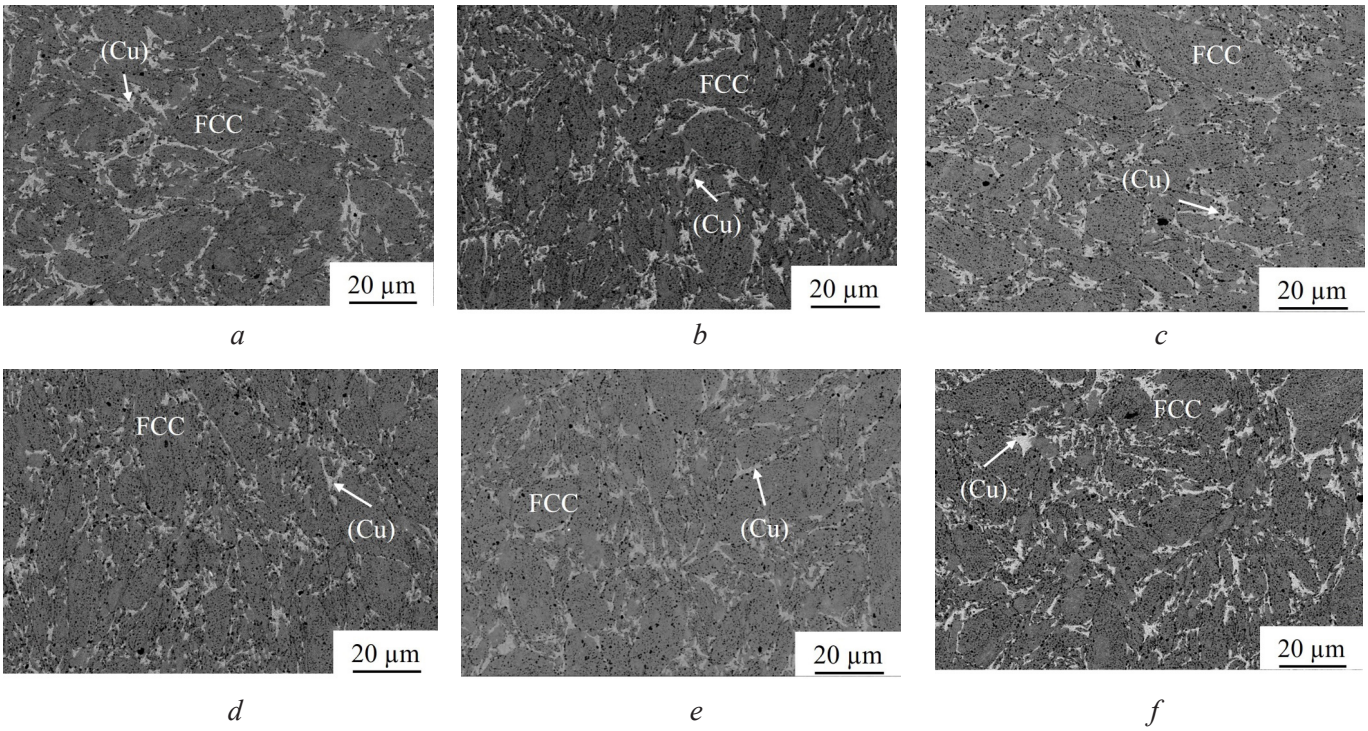

Fig. 3. SEM images of the *CoCrCuFeNi* (*a*, *b*), *CoCrCuFeNi*–0.4*C* (*c*, *d*), and *CoCrCuFeNi*–1.0*C* (*e*, *f*) HEAs. Images (*a*, *c*, *e*) show the microstructures after *HP*, while images (*b*, *d*, *f*) show the microstructures after *HP* and *HT*

For a detailed study of the grain size, morphology, and distribution of carbide phases, as well as for the evaluation of the dislocation substructure, *TEM* analysis was performed on the *CoCrCuFeNi–1.0C* alloy in two conditions: after *HP* and after *HP + HT*. The results are shown in Figs. 4 and 5, respectively.

Bright-field images (Fig. 4,*a*; Fig. 5,*a*) show that the *FCC* matrix of the alloy has an ultrafine-grained (*UFG*) structure. The average crystallite size, determined by the intercept method, is 620 ± 50 nm after *HP* and increases to 840 ± 70 nm after *HT*. This moderate grain growth (approximately 35%) indicates that carbide particles located at grain boundaries effectively retard grain boundary migration, but do not completely block it.

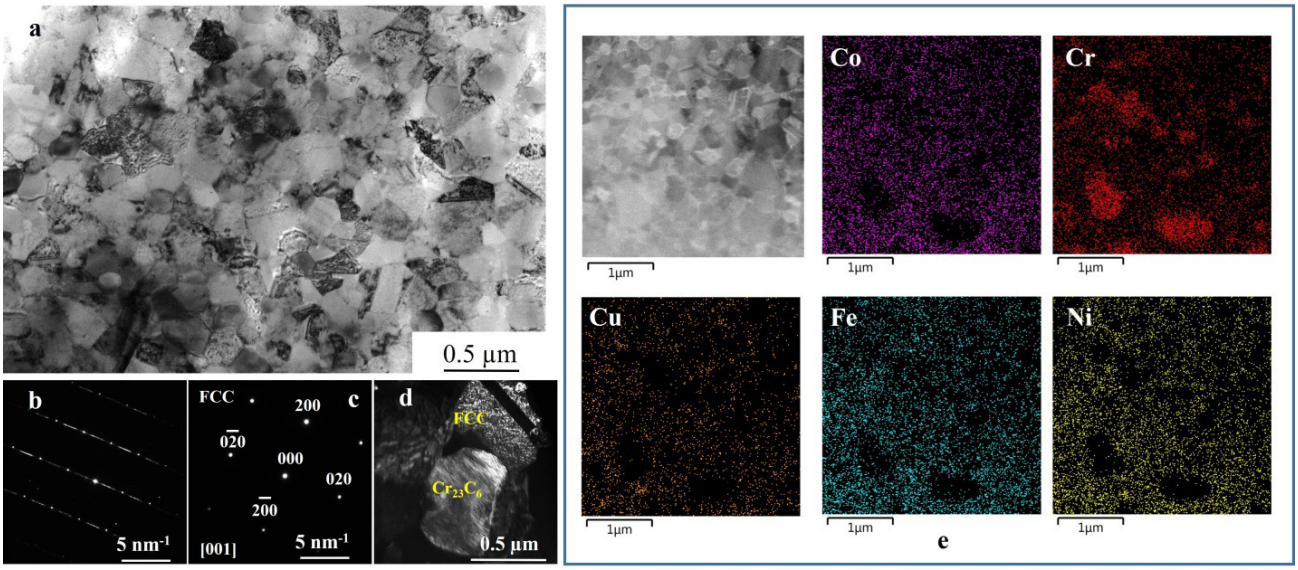

Fig. 4. TEM images of the microstructure of the *CoCrCuFeNi–1.0C* (*HP*) *HEA* (*a*), *SAED* patterns from $Cr_{23}C_6$ (*b*) and *FCC* (*c*) grains; a dark-field image of the structure (*d*), and *EDS* elemental distribution maps (*e*)

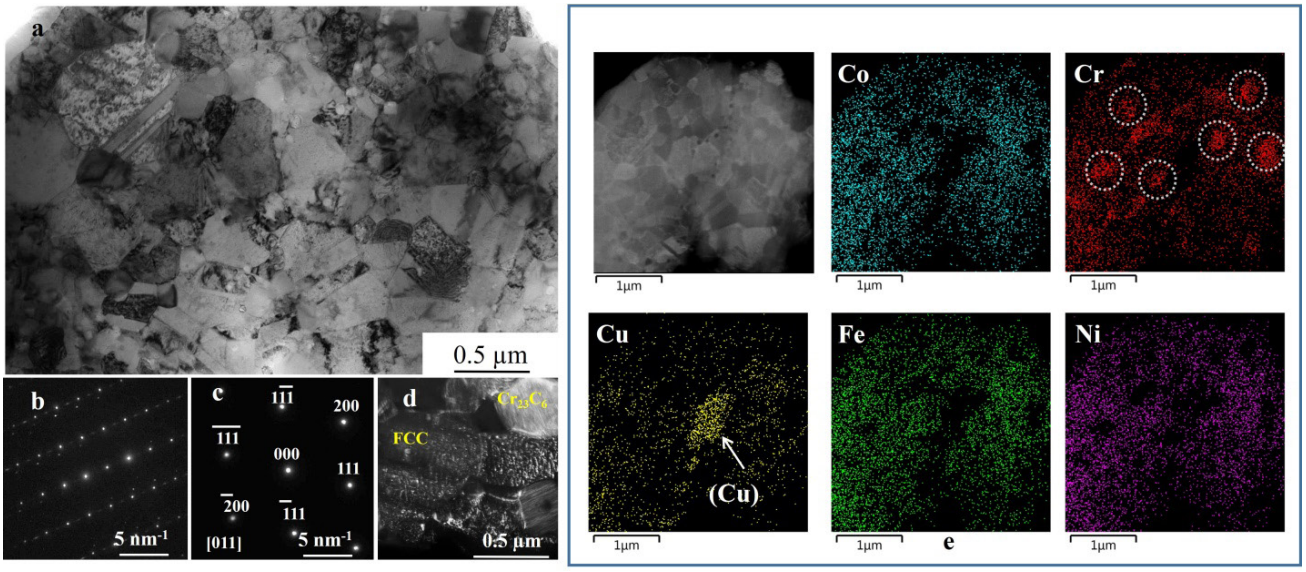

Fig. 5. TEM images of the microstructure of the *CoCrCuFeNi–1.0C* (*HP+HT*) *HEA* (*a*), *SAED* patterns from $Cr_{23}C_6$ (*b*) and *FCC* (*c*) grains; a dark-field image of the structure (*d*), and *EDS* elemental distribution maps (*e*)

Since the matrix grains and carbide phases are not distinguished by contrast in bright-field *TEM* images, *EDS* mapping (Fig. 4,*d*; Fig. 5,*d*) and microdiffraction (Fig. 4,*b*, *c*; Fig. 5,*b*, *c*) were used for their identification. According to elemental distribution maps, chromium is localized in uniformly distributed regions of submicron size. Analysis of electron diffraction patterns allows these regions to be unambiguously identified as chromium carbide $Cr_{23}C_6$.

An important feature is the predominant localization of carbides at the grain boundaries of the *FCC* matrix. The size of the carbide grains is comparable with that of the matrix grains (hundreds of nanometers). Such an arrangement of carbides suggests that they serve two functions: pinning grain boundaries with the restriction of grain growth during high-temperature processing and increasing the resistance of grain boundaries to dislocation slip, which may affect deformation and fracture mechanisms.

Dark-field *TEM* images (Fig. 4,*d*; Fig. 5,*d*) indicate a high dislocation density in the *FCC* solid solution. After *HT*, the dislocation density remains visually high, suggesting that no significant stress relaxation occurs, which is consistent with the calculations by the *Williamson–Hall* method. Dislocations are distributed relatively uniformly throughout the grain volume, without forming a distinct cell structure.

TEM examination of deformed specimens revealed isolated deformation twins; however, their number was insignificant, and they did not exert a determining influence on the ductility of the alloys. The suppression of the *TWIP* effect is attributed to the fact that in *UFG* materials the critical stress for twin nucleation is high, and grain boundaries become effective sinks for dislocations, hindering the accumulation of defects required to initiate twinning.

A comparison of Figs. 4 and 5 shows that *HT* at 900 °C leads to the following changes: an increase in the average grain size of the *FCC* matrix, a slight coarsening of carbide particles (without altering their predominant localization at grain boundaries), and retention of a high dislocation density.

The study of the mechanical properties of *CoCrCuFeNi HEAs* with different carbon content (Table 3) revealed the following features.

Table 3

Mechanical properties of the *CoCrCuFeNi*-based *HEAs* after *HP* and *HP* + *HT*

Composition	Hardness, GPa		σ_b, MPa	
	HP	HP + HT	HP	HP + HT
CoCrCuFeNi	3.27 ± 0.12	3.15 ± 0.15	1440 ± 80	1450 ± 50
CoCrCuFeNi–0.2C	3.37 ± 0.18	3.34 ± 0.18	1480 ± 90	1560 ± 40
CoCrCuFeNi–0.4C	3.30 ± 0.15	3.20 ± 0.20	1520 ± 80	1720 ± 40
CoCrCuFeNi–0.6C	3.20 ± 0.20	3.00 ± 0.12	1470 ± 90	1680 ± 80
CoCrCuFeNi–0.8C	3.48 ± 0.13	3.15 ± 0.12	1530 ± 30	1630 ± 30
CoCrCuFeNi–1.0C	3.56 ± 0.12	3.25 ± 0.12	1620 ± 70	1780 ± 50

At carbon contents below 0.6%, the hardness of the alloys after *HP* increases non-monotonically. This may be attributed to the competition between two opposing processes: chromium depletion of the matrix, which reduces hardness, and carbide strengthening, which provides the opposite effect. Upon addition of 0.8–1.0% *C*, the contribution of carbide strengthening prevails, resulting in an increase in hardness to 3.48–3.56 GPa. *HT* leads to a slight decrease in hardness (by 5–10%), which is associated with partial relaxation of internal stresses and moderate grain growth. However, as shown by dark-field *TEM* images (Fig. 4,*d*; Fig. 5,*d*) , the dislocation density remains high after *HT*, so the hardness drop does not exceed 10%.

In three-point bending tests, an increase in bending strength $\boldsymbol{\sigma_\beta}$ with increasing carbon content was observed. The highest effect is achieved by the combined application of carbon alloying and *HT*: for the *CoCrCuFeNi–1.0C* alloy after *HT*, $\boldsymbol{\sigma_b}$ reaches 1,780 MPa, which is 23.6% higher than that of the unalloyed alloy without *HT* (1,440 MPa). The increase in $\boldsymbol{\sigma_b}$ after *HT* is attributed to two factors. First, *HT* promotes further reaction of the remaining dissolved carbon with the formation of additional carbides (Table 1). Carbide particles, by pinning grain boundaries, hinder their migration and contribute to the retention of the *UFG* structure. Second, a moderate increase in grain size (from 620 to 840 nm) reduces the specific area of grain boundaries. Since *UFG* materials are prone to intergranular fracture, a reduction in the total grain boundary area has a positive effect on crack propagation resistance. Thus, the negative effect of grain growth according to the *Hall–Petch* relationship is compensated by an increase in fracture toughness.

Fig. 6 presents the stress–strain curves for the *CoCrCuFeNi* alloys with 0, 0.2, 0.4, 0.6, 0.8, and 1.0 wt.% *C* after *HP* + *HT*, together with the curve for the base alloy after *HP*. The base alloy fractures in a brittle manner, showing virtually no plastic deformation. Its ultimate strength is 580 MPa after HP and 730 MPa after *HP* + *HT*, and the fracture surface exhibits a cleavage pattern (Fig. 7,*a*), consistent with the absence of a nonlinear region on the curve. As the carbon content rises, the deformation curves develop nonlinear segments and the ultimate tensile strength (*UTS*) increases. The alloy with 1% *C* reaches *UTS* of 1,010 MPa and a residual strain of about 2.3%. Fractographic examination (Fig. 7,*b*) reveals a ductile fracture mode, evidenced by a dimpled microstructure.

Classical strengthening mechanisms fail to explain the observed simultaneous increase in strength and ductility. *TEM* data show that the average grain size rises from 620 to 840 nm after heat treatment – yet the

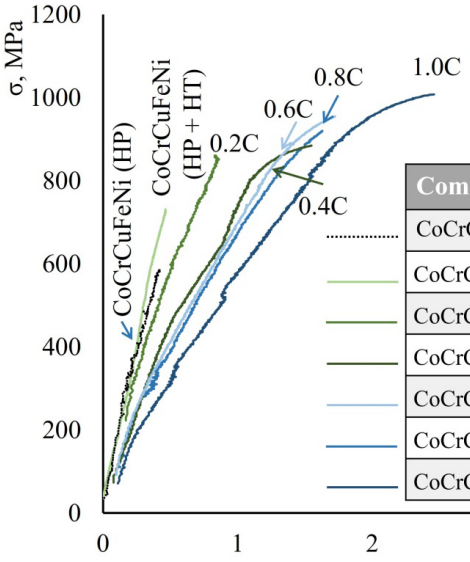

Composition	σ, MPa	ε, %
CoCrCuFeNi (HP)	580 ± 30	0.35 ± 0.10
CoCrCuFeNi (HP + HT)	730 ± 30	0.40 ± 0.10
CoCrCuFeNi-0.2C	830 ± 10	0.65 ± 0.20
CoCrCuFeNi-0.4C	930 ± 10	1.23 ± 0.20
CoCrCuFeNi-0.6C	885 ± 5	1.55 ± 0.15
CoCrCuFeNi-0.8C	925 ± 30	1.70 ± 0.10
CoCrCuFeNi-1.0C	1010 ± 5	2.30 ± 0.10

Fig. 6. Stress–strain curves of the *CoCrCuFeNi HEAs* (after *HP* and *HP* + *HT*) with carbon addition (after *HP* + *HT*), obtained from uniaxial tensile tests

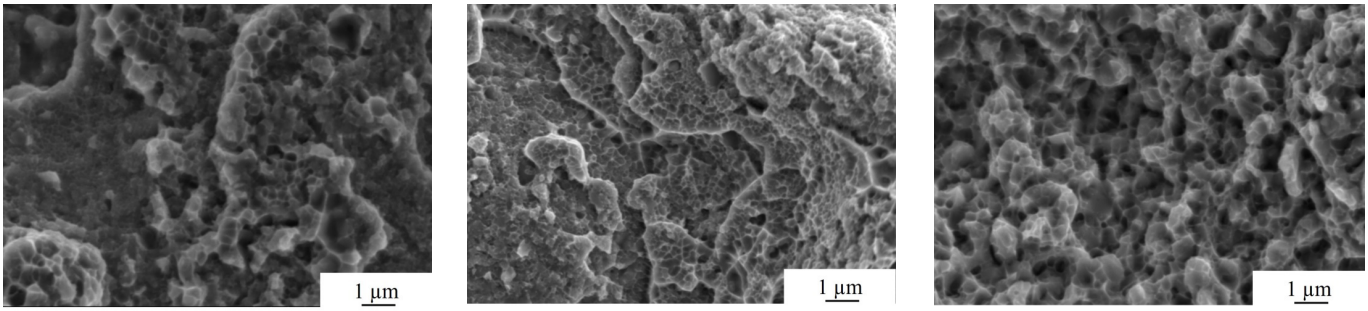

a *b* *c*

Fig. 7. Fractographs of the *CoCrCuFeNi* (a), *CoCrCuFeNi–0.6C* (*b*), and *CoCrCuFeNi–1.0C* (*c*) *HEAs*

Hall–Petch relationship would predict a strength decrease from such grain growth. Dispersion strengthening via the *Orowan* mechanism also cannot account for the effect, because the carbide particles reside predominantly at grain boundaries, not inside the grains. *XRD* analysis using the *Williamson–Hall* method reveals that the dislocation density drops from 8.8×10^{13} to 4.7×10^{13} m^{-2} after *HT*, which rules out dislocation strengthening as the main contributor. Finally, the lattice parameter of the *FCC* matrix remains unchanged upon carbon addition, indicating that solid solution strengthening plays a negligible role.

The main benefit of combining carbon alloying with *HT*, therefore, lies not in creating new obstacles for dislocations, but in enhancing fracture toughness. Heat treatment binds the remaining dissolved carbon into carbides, which reduces matrix embrittlement. At the same time, it reduces the total grain boundary area. For *UFG* materials that are susceptible to intergranular fracture, this effect is critically important. The cohesive strength of grain boundaries increases, and stress concentrations diminish. As a result, the material can exploit its inherent strength potential – provided by the *UFG* structure – which was previously limited by brittleness.

Fractographic analysis of *CoCrCuFeNi HEAs* with different carbon content revealed distinct fracture modes that correlate with the mechanical properties presented in Table 2 and Fig. 6. Fig. 7,*a* shows the fracture surface of the base *CoCrCuFeNi* alloy. The surface exhibits a typical morphology of brittle fracture: smooth cleavage facets with low roughness dominate, and no signs of plastic deformation are visible. This fracture type indicates that cracks propagate predominantly along grain boundaries (intergranular fracture) or along cleavage planes within the grains. A small fraction of areas with a dimpled microstructure suggests that the base alloy cannot undergo significant plastic deformation prior to failure, which is consistent with the linear deformation curve in Fig. 6 and the low residual strain values.

The fracture surface of the *CoCrCuFeNi–0.6C* alloy (Fig. 7,*b*) exhibits an intermediate morphology. Dimpled regions are present, but the dimples themselves are mostly located on relatively flat cleavage facets. This indicates a mixed fracture mode, where local plastic deformation within individual microvolumes does not lead to a fully ductile fracture, owing to insufficient grain boundary pinning by carbide particles. This morphology correlates well with the intermediate mechanical properties of this composition (Table 3) and points to a transitional fracture behavior – from brittle cleavage to ductile transgranular fracture – as the carbon content increases.

In contrast, the fracture surface of the *CoCrCuFeNi–1.0C* alloy (Fig. 7,*c*) shows a typical dimpled structure indicating ductile transgranular fracture. The dimples form through the nucleation, growth, and coalescence of micropores, which initiate predominantly at carbide particles or other structural heterogeneities. The size and depth of the dimples reflect the degree of ductility: relatively fine and shallow dimples (Fig. 7,*c*) correspond to moderate ductility (residual strain of 2.3% from Fig. 6), yet they differ fundamentally from the completely brittle fracture of the base alloy. The transition from brittle cleavage to ductile dimple fracture upon alloying with 1 wt.% carbon and subsequent *HT* is attributed to the formation of carbide phases that pin grain boundaries and promote stress redistribution, as well as to the reduction in dissolved carbon in the matrix, which lessens its embrittlement.

Tribological tests were performed only for the two extreme compositions (the base alloy and *CoCrCuFeNi–1.0C*), based on the results of the mechanical tests. These two states exhibit the most contrasting deformation behavior – brittle and ductile fracture.

The tribological test results (Table 4, Fig. 8) show that the coefficient of friction depends weakly on the composition and processing condition, remaining within a narrow range of 0.75–0.77 (Fig. 8,*a*). All specimens display a prolonged running-in period (about 2,000 cycles), after which the coefficient of friction stabilizes at around 0.80. This behavior may arise from wear of the spherical counterbody and the consequent increase in contact area, as well as from compaction of wear debris and its gradual removal from the contact zone. This friction coefficient trend is consistent with the results reported in [9]. On the friction coefficient curves for the base alloy after *HT*, local spikes are observed, which are likely associated with periodic spalling of oxide films that form in the contact zone.

The specific wear rate varies slightly with the *HEA* structure. The *CoCrCuFeNi* alloy exhibits the lowest specific wear rate of 7.01×10^{-5} mm^3/(N·m). After *HT* at 900 °C, the wear rate increases to 10.54×10^{-5} mm^3/(N·m), which may be attributed to relaxation of the *FCC* phase. In addition, increased material pile-up along the edges of the wear track (Fig. 8,*a*) suggests a reduction in the alloy's resistance to plastic deformation as a result of *HT*.

The introduction of 1 wt.% carbon into the *CoCrCuFeNi* alloy results in the formation of carbides. Despite the maximum hardness of 3.56 GPa, this is accompanied by an increase in the specific wear rate to 10.21×10^{-5} mm^3/(N·m). Upon *HT* of this alloy, the specific wear rate decreases to a minimum value of 7.10×10^{-5} mm^3/(N·m). This change may be associated with improved deformability of the matrix and its enhanced resistance to local fracture during friction. The more ductile deformation behavior after *HT* is confirmed by the dimpled fracture morphology (Fig. 7,*b*) and the residual strain in tensile tests (2.3%).

Table 4

Tribological properties of the studied *HEAs*

Composition	Production route	Specific wear, ($\times 10^{-5}$ mm^3/(N·m))		Coefficient of friction	
		specimen	counterbody	Average	Final
CoCrCuFeNi	*HP*	7.01	0.79	0.77	0.81
CoCrCuFeNi	*HP + HT*	10.54	0.95	0.77	0.87
CoCrCuFeNi–1.0C	*HP*	10.21	0.80	0.75	0.81
CoCrCuFeNi–1.0C	*HP + HT*	7.10	1.18	0.77	0.81

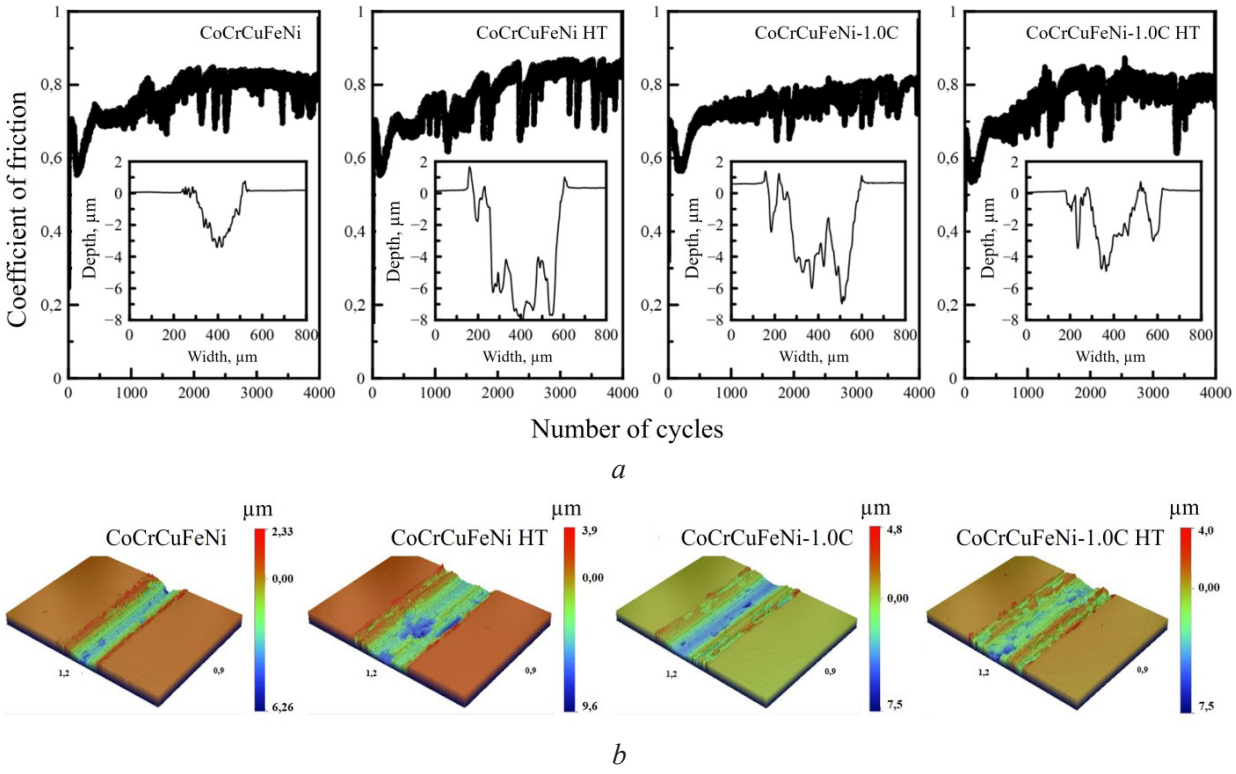

Fig. 8. Friction coefficient as a function of the number of cycles and 2D (*a*) and 3D (*b*) images of wear tracks of the *CoCrCuFeNi–xC HEAs*

In addition to specimen wear, the behavior of the counterbody (Si_3N_4 ball) is also of interest. For the *CoCrCuFeNi–1.0C* composition after *HT*, the maximum counterbody wear is observed (1.18×10^{-5} mm^3/(N·m)) , whereas for the base alloy this parameter is substantially lower ($0.79–0.95 \times 10^{-5}$ mm^3/(N·m)). This difference is attributed to the fact that the surface of the *CoCrCuFeNi–1.0C* alloy after *HT*, being strengthened by carbides, acts as a more aggressive abrasive, intensifying the wear of the ceramic counterbody.

Conclusions

1. Mechanical alloying followed by hot pressing was found to ensure the formation of homogeneous *CoCrCuFeNi–xC* powder mixtures (***x*** = 0.2, 0.4, 0.6, 0.8, 1.0 wt.%) and to yield compact specimens with a two-phase structure consisting of an *FCC* solid solution and a copper-enriched phase (*Cu*). The addition of carbon in the range of 0.2–1.0 wt.% does not appreciably alter the phase ratio of the *FCC* and (*Cu*) phases, but leads to the formation of chromium carbides $Cr_{23}C_6$ and $Cr_2(C,N)$.

2. Carbon proved to be an effective alloying addition for strengthening the *CoCrCuFeNi* alloy: hardness increases from 3.27 to 3.56 GPa, and bending strength rises from 1,440 ± 80 to 1,620 ± 70 MPa as the carbon content increases to 1.0 wt.%. After additional heat treatment, the maximum bending strength reaches 1,780 ± 50 MPa for the *CoCrCuFeNi–1.0 C* alloy. According to *TEM* data, the matrix of the alloy with 1.0 wt.% *C* has an ultrafine-grained structure: the average crystallite size ranges from 620 ± 50 to 840 ± 70 nm depending on the processing condition, with carbide particles predominantly located at grain boundaries.

3. The combination of carbon addition and subsequent heat treatment allows the deformation behavior of the alloys to be modified. The base *CoCrCuFeNi* alloy fractures in a brittle mode, with no evidence of plastic deformation, and shows a tensile strength of about 730 MPa. By contrast, the *CoCrCuFeNi–1.0 C* alloy following *HT* exhibits a tensile strength of 1,010 MPa and a residual strain of 2.3%.

3. Carbon alloying of the *HEA* and subsequent annealing were shown to have only a minor effect on the coefficient of friction under dry sliding against Si_3N_4 ceramics, which remains within a narrow range of 0.75–0.77. A reduction in the specific wear rate of the *HEA* is observed at a carbon content of 1 wt.% and after annealing in a hydrogen atmosphere (***T*** = 900 °C) , owing to the increased fracture toughness of the matrix.

References

1. Yeh J.-W., Chen S.-K., Lin S.-J., Gan J.-Y., Chin T.-S., Shun T.-T., Tsau C.-H., Chang S.-Y. Nanostructured high-entropy alloys with multiple principal elements: Novel alloy design concepts and outcomes. *Advanced Engineering Materials*, 2004, vol. 6 (5), pp. 299–303. DOI: 10.1002/ADEM.200300567.

2. Cantor B., Chang I.T.H., Knight P., Vincent A.J.B. Microstructural development in equiatomic multicomponent alloys. *Materials Science and Engineering A*, 2004, vol. 375–377, pp. 213–218. DOI: 10.1016/J.MSEA.2003.10.257.

3. Jiao H., Zhong D., Peng B., Mei M., Xu N., Misra R.D.K., Tang Y., Zhao L.-Z. Enhanced strength-ductility synergy in $Fe_{50}Mn_{30}Co_{10}Cr_{10}$ high-entropy alloy with multi-scale nanotwins. *Materials Science and Engineering A*, 2026, vol. 949, p. 149447. DOI: 10.1016/J.MSEA.2025.149447.

4. Li J., Feng K., Zhou F., Qin Q., Yu T., Zhao H., Ge L. Enhanced strength-ductility synergy in a Cu-based high entropy alloy via severe cold-deformed and annealing treatment. *Journal of Materials Research and Technology*, 2025, vol. 39, pp. 7717–7731. DOI: 10.1016/J.JMRT.2025.11.133.

5. Wang S., Chen Z., Chen R., Wu Z., Jia Y., Zhang W., Wang Y., Liu W., Zhao Y., Shi R., Cao B., Yu S., Wei J. Superior strength-ductility synergy in additively manufactured CoCrFeNi high-entropy alloys with multi-scale hierarchical microstructure. *Journal of Alloys and Compounds*, 2024, vol. 1006, p. 176268. DOI: 10.1016/J.JALLCOM.2024.176268.

6. Wang P., Chen C., Pu Z., Xu Z.-L., Chan K. Enhanced strength-ductility synergy in complex hetero-structured eutectic high entropy alloy via multi-mechanism deformation. *Journal of Materials Science and Technology*, 2026, vol. 265, pp. 235–255. DOI: 10.1016/J.JMST.2025.11.024.

7. Maharana S., Biswal S., Sabat M., Prasad D.K.V.D., Laha T. Deciphering the role of stacking fault energy on TWIP–TRIP interplay in Ni-rich high entropy alloy with tailored Ti content. *International Journal of Plasticity*, 2026, vol. 199, p. 104642. DOI: 10.1016/J.IJPLAS.2026.104642.

8. Loginov P.A., Fedotov A.D., Mukanov S.K., Manakova O.S., Zaitsev A.A., Akhmetov A.S., Rupasov S.I., Levashov E.A. Manufacturing of metal–diamond composites with high-strength $CoCrCu_xFeNi$ high-entropy alloy used as a binder. *Materials*, 2023, vol. 16 (3), p. 1285. DOI: 10.3390/MA16031285.

9. Mukanov S., Loginov P., Fedotov A., Bychkova M., Antonyuk M., Levashov E. The effect of copper on the microstructure, wear and corrosion resistance of CoCrCuFeNi high-entropy alloys manufactured by powder metallurgy. *Materials*, 2023, vol. 16 (3), p. 1178. DOI: 10.3390/MA16031178.

10. Kuptsov K.A., Antonyuk M.N., Sheveyko A.N., Bondarev A.V., Ignatov S.G., Slukin P.V., Dwivedi P., Fraile A., Polcar T., Shtansky D.V. High-entropy Fe-Cr-Ni-Co-(Cu) coatings produced by vacuum electro-spark deposition for marine and coastal applications. *Surface and Coatings Technology*, 2023, vol. 453, p. 129136. DOI: 10.1016/J.SURFCOAT.2022.129136.

11. Fatykhova M.N., Kuptsov K.A., Sheveyko A.N., Gizatullina A.R., Loginov P.A., Shtansky D.V. High-entropy Fe-Co-Cr-Ni-(Cu) coatings with enhanced corrosion and tribocorrosion resistance obtained by vacuum electrospark deposition. *Izvestiya vuzov. Tsvetnaya metallurgiya = Izvestiya. Non-Ferrous Metallurgy*, 2024, vol. 30, no. 3, pp. 87–96. DOI: 10.17073/0021-3438-2024-3-87-96. (In Russian).

12. Burla A., Khandelwal M., Vaidya M. Antibacterial properties of Cu containing complex concentrated alloys. *Materials Today Communications*, 2022, vol. 33, p. 104915. DOI: 10.1016/J.MTCOMM.2022.104915.

13. Guo T., Li J., Wang J., Wang Y., Kou H., Niu S. Liquid-phase separation in undercooled CoCrCuFeNi high entropy alloy. *Intermetallics*, 2017, vol. 86, pp. 110–115. DOI: 10.1016/J.INTERMET.2017.03.021.

14. Yu P., Lin C.M., Kou S. Microstructure evolution of a CoCrFeNiCu high entropy alloy in directional solidification by arc welding and quenching. *Journal of Alloys and Compounds*, 2025, vol. 1039, p. 183228. DOI: 10.1016/J.JALLCOM.2025.183228.

15. Li N., Jia C.L., Wang Z.W., Wu L.-H., Ni D.R., Li Z.-K., Fu H., Xue P., Xiao B.-L., Ma Z.Y., Shao Y., Chang Y.-L. Achieving a high-strength CoCrFeNiCu high-entropy alloy with an ultrafine-grained structure via friction stir processing. *Acta Metallurgica Sinica (English Letters)*, 2020, vol. 33 (7), pp. 947–956. DOI: 10.1007/S40195-020-01037-9.

16. Thangaraju S., Bouzy T.E., Hazotte A. Phase stability of a mechanically alloyed CoCrCuFeNi high entropy alloy. *Advanced Engineering Materials*, 2017, vol. 19 (8), p. 1700095. DOI: 10.1002/ADEM.201700095.

17. Hu Q., Wang H.L., Qian L.H., Zeng L.-c., Wang Q., Liu X.-w. Effects of Cu additions on microstructure and mechanical properties of as-cast CrFeCoNiCux high-entropy alloy. *Transactions of Nonferrous Metals Society of China*, 2023, vol. 33 (6), pp. 1803–1813. DOI: 10.1016/S1003-6326(23)66223-5.

18. Fedotov A.D., Mukanov S.K., Romanenko B.Yu., Loginov P.A., Bychkova M.Ya., Rupasov S.I. Mechanical and tribological characteristics of nickel-rich $CoCrCu_xFeNi_2$ high entropy-alloys. *Izvestiya vysshikh uchebnykh*

zavedenii. Tsvetnaya metallurgiya = Izvestiya. Non-Ferrous Metallurgy, 2024, vol. 30, no. 1, pp. 55–69. DOI: 10.17073/0021-3438-2024-1-55-69.

19. Narzulloev U.U., Matveev A.T., Kaplanskaya L.Y., Mukanov S., Kuptsov K., Teplyakova T., Loginov P., Shchetinin I., Shtansky D. Boron-doped high entropy CrFeCoNiCu alloy-based composites reinforced with oxides and borides with enhanced thermomechanical properties. *Journal of Alloys and Compounds*, 2025, vol. 1036, p. 181778. DOI: 10.1016/J.JALLCOM.2025.181778.

20. Astafurova E.G., Reunova K.A., Melnikov E.V., Panchenko M.Yu., Astafurov S.V., Maier G.G., Moskvina V.A. On the difference in carbon- and nitrogen-alloying of equiatomic FeMnCrNiCo high-entropy alloy. *Materials Letters*, 2020, vol. 276, p. 128183. DOI: 10.1016/J.MATLET.2020.128183.

21. Astafurov S.V., Melnikov E.V., Reunova K.A., Panchenko M.Yu., Zagibalova E.A., Krukovskii K.V., Astafurova E.G. The way to improve strength and ductility of heavily carbon-alloyed high-entropy $Fe_{20}Mn_{20}Cr_{20}Ni_{20}Co_{15}C_5$ alloy. *Materials Science and Engineering A*, 2022, vol. 851, p. 143628. DOI: 10.1016/J.MSEA.2022.143628.

22. Astafurova E.G., Reunova K.A., Astafurov S.V., Astapov D.O. Temperature dependence of the deformation behavior of high-entropy alloys $Co_{20}Cr_{20}Fe_{20}Mn_{20}Ni_{20}$, $Co_{19}Cr_{20}Fe_{20}Mn_{20}Ni_{20}C_1$, and $Co_{17}Cr_{20}Fe_{20}Mn_{20}Ni_{20}C_3$. Mechanical properties and temperature dependence of yield stress. *Physical Mesomechanics*, 2024, vol. 27, pp. 113–123. DOI: 10.1134/S1029959924020012.

23. Astafurova E.G., Melnikov E.V., Reunova K.A., Astafurov S., Panchenko M., Mikhno A., Tumbusova I. Temperature dependence of mechanical properties and plastic flow behavior of cast multicomponent alloys $Fe_{20}Cr_{20}Mn_{20}Ni_{20}Co_{20-x}C_x$ (x = 0, 1, 3, 5). *Physical Mesomechanics*, 2021, vol. 24, pp. 674–683. DOI: 10.1134/S1029959921060059.

24. Wang Q.K., Li S.A., He L.X., Wang Z.K., Cai Y., Zhang N., Zhao X.J., Lu L. Synergistic enhancement of strength and ductility of CoCrNi medium-entropy alloy via dual carbon-induced heterogeneous structures. *Materials Science and Engineering A*, 2025, vol. 948, p. 149317. DOI: 10.1016/j.msea.2025.149317.

25. Amani-Ghadim H., Farjam R., Akbari A. Carbon doped $Co_{40}Cr_{20}Ni_{20}Fe_{10}Mn_{10}$ high entropy alloy: microstructure and mechanical properties. *High Entropy Alloy Materials*, 2026, vol. 2026, pp. 1–19. DOI: 10.1007/S44210-025-00073-3.

26. Ma K., Feng L., Liu J., Zhao Y. Microstructure and compressive deformation behavior of carbon-doped Fe0.5CrMnAlCu high-entropy alloy. *Journal of Alloys and Compounds*, 2025, vol. 1046, p. 184880. DOI: 10.1016/J.JALLCOM.2025.184880.

27. Tang Q., Peng S., Lin C., Hou Y., Chen L., Li Z. Overcoming the strength-ductility trade-off of additively manufactured metastable high-entropy alloy via carbon doping. *Journal of Alloys and Compounds*, 2025, vol. 1036, p. 181960. DOI: 10.1016/J.JALLCOM.2025.181960.

28. Fedotov A.D., Mukanov S.K., Rupasov S.I., Loginov P.A., Levashov E.A. Poluchenie iznosostoikikh boridnykh kermetov na osnove vysokoentropiinogo splava CoCrCuFeNi metodom goryachego pressovaniya [Production of wear-resistant boride cermets based on the high-entropy CoCrCuFeNi alloy by hot pressing]. *Metallurg = Metallurgist*, 2026, no. 1, pp. 93–102. DOI: 10.52351/00260827_2026_1_93.

29. Wang Z., Baker I., Cai Z., Chen S., Poplawsky JD., Guo W. The effect of interstitial carbon on the mechanical properties and dislocation substructure evolution in Fe40.4Ni11.3Mn34.8Al7.5Cr6 high entropy alloys. *Acta Materialia*, 2016, vol. 120, pp. 228–239. DOI: 10.1016/j.actamat.2016.08.072.

30. Wu Z., He M., Cao H., Wang S., Chen R., Cao B., Shi R., Liu X., Yu S., Wang S., Bai J., Wei J. Ultrahigh-strength and ductile CoCrFeNi-based high-entropy alloys manufactured by laser powder bed fusion with multiple strengthening mechanisms. *Journal of Materials Research and Technology*, 2023, vol. 25, pp. 2948–2960. DOI: 10.1016/j.jmrt.2023.06.110.

31. Nam S., Hwang J.Y., Jeon J., Park J., Bae D., Kim M.J., Kim J.H., Choi H. Deformation behavior of nanocrystalline and ultrafine-grained CoCrCuFeNi high-entropy alloys. *Journal of Materials Research*, 2019, vol. 34 (5), pp. 720–731. DOI: 10.1557/JMR.2018.477.

Conflicts of Interest

The authors declare no conflict of interest.